

A Priori Assessment of the Two-Level Simulation Model for Simulation of Turbulent Non-Premixed Flames

R. Smith* and R. Ranjan†

Numerical investigation of turbulent combustion tends to be challenging from the computational cost perspective due to the need to accurately capture the multi-scale and nonlinear processes resulting from turbulence-chemistry interaction. Therefore, a reliable and robust modeling strategy is needed for efficient simulation of turbulent combustion. In this study, we assess the performance of the two-level simulation (TLS) modeling strategy for the simulation of turbulent non-premixed combustion. In the TLS model, which was originally developed for incompressible turbulent flows and scalar mixing in such flows, both large- and small-scale flow fields are explicitly evolved in a coupled manner. An extensive *a priori* assessment of the TLS model is performed using the direct numerical simulation dataset corresponding to a temporally evolving turbulent non-premixed jet flame, which exhibits the presence of extinction and re-ignition phenomena, making it a challenging test case for model assessment. The *a priori* analysis is carried out by examining the behavior of the large- and the small-scales of the reacting flow field in the physical and the spectral space and verifying the TLS modeling assumptions that are used to simplify the small-scale equations.

I. Introduction

Numerical investigation of turbulent combustion can be performed using approaches with different levels of fidelity. For example, direct numerical simulation (DNS), where all the relevant scales are captured, is typically used for the investigation of fundamental features of turbulence-chemistry interaction. However, the large computational cost of DNS limits its usage to simplified geometries and lower-to-moderate Reynolds number (Re) flows. Large-eddy simulation (LES), on the other hand, appears to be a viable alternative for the simulation of practically relevant flows, where the large-scale (LS) features are captured and the effects of small-scale (SS) features are modeled using SGS closures [1, 2]. However, the employed SGS closures should be accurate and robust enough to account for the SS processes (reaction, diffusion, and mixing) and their coupling with the LS processes. In this study, we focus on a multi-scale modeling strategy for the simulation of turbulent non-premixed flames within the finite-rate kinetics framework.

Although there exists a wide range of SGS models for turbulent combustion, there are challenges in terms of their regime of applicability, the ability to account for finite-rate kinetics effects, handling of different modes of turbulent combustion (premixed and non-premixed), etc. These challenges have led to the development of numerous SGS closures such as partially stirred reactor (PaSR) [3], thickened flame model (TFM) [4], flame surface density (FSD) [5], conditional moment closure (CMC) [6], conditional source estimation (CSE) [7], transported probability density function (TPDF) [8], multi-environment PDF (MEPDF) [9], one-dimensional turbulence (ODT) [10], and linear-eddy model (LEM) [11] and its variants [12, 13], etc. Despite the availability of a wide range of models, the establishment of an SGS model that works for all regimes and over a range of operating conditions without *ad hoc* tuning is still needed. The present study focuses on the assessment of the TLS model, which has unique capabilities to explicitly account for LS and SS processes, and a coupling of such processes.

TLS is a multi-scale model [14], which was originally developed for the simulation of high Re turbulent flows. It applies the scale decomposition directly to the Navier-Stokes equations leading to governing equations for both the large- and small-scales of motion. The coupled LS and SS equations are simplified further by employing the TLS modeling assumptions to the SS equations. Additionally, to reduce computational costs, the three-dimensional (3D) SS equations are solved on three orthogonal one-dimensional (1D) lines embedded within a 3D grid on which the LS equations are solved. As the TLS model simulates both LS and SS processes and their interactions, it has some unique physics-based capabilities in capturing the SS physics such as vorticity dynamics, scalar dissipation rate, anisotropic behavior, co-/counter-gradient transport, backscatter, etc. [15, 16]. Some of these small-scale features are difficult to capture while employing a conventional LES relying on eddy viscosity/diffusivity based modeling strategy. TLS model

*GRA, Department of Mechanical Engineering, The University of Tennessee Chattanooga, AIAA Student Member, 1346001.

†Assistant Professor, Department of Mechanical Engineering, The University of Tennessee Chattanooga, AIAA Senior Member, 480307.

has been extensively used in the past studies to study a wide range of flows such as isotropic turbulence, temporal mixing layer, wall-bounded flows, transitional flows, compressible scalar mixing, etc [14, 16–23]. The model has been recently extended for the modeling of passive scalar mixing [15]. In a recent study, the *a priori* assessment of the model for turbulent premixed flames have shown its promising abilities [24]. The present study focuses on assessing the capabilities of this model in capturing the features of turbulent non-premixed flames. We consider a temporally evolving turbulent non-premixed jet flame which exhibits the approach towards extinction followed by re-ignition, thus posing a challenging task from a modeling perspective. Note that this configuration has been extensively studied in the past for the development and assessment of novel methods and models [25, 26].

This article is arranged as follows. Section II describes the governing equations and the formulation of the TLS model. Section III discusses the computational setup and the numerical approach. The results from the analysis of the model are discussed in Sec. IV. Finally, a summary of the key conclusions of this study is presented in Sec. V.

II. Mathematical Formulation

In this section, we first describe the governing equations. Afterward, details of the TLS model and the resulting LS and SS governing equations are presented.

A. Governing equations

The governing equations for turbulent combustion comprise the compressible multi-species reacting Navier-Stokes equations, which correspond to the conservation of mass, momentum, energy, and species mass. These equations are given by

$$\frac{\partial \rho}{\partial t} + \frac{\partial \rho u_i}{\partial x_i} = 0, \quad (1)$$

$$\frac{\partial \rho u_i}{\partial t} + \frac{\partial}{\partial x_j} [\rho u_i u_j + P \delta_{ij} - \tau_{ij}] = 0, \quad (2)$$

$$\frac{\partial \rho E}{\partial t} + \frac{\partial}{\partial x_i} [(\rho E + P)u_i + q_i - u_j \tau_{ij}] = 0, \quad (3)$$

$$\frac{\partial \rho Y_k}{\partial t} + \frac{\partial}{\partial x_i} [\rho (Y_k u_i + Y_k V_{i,k})] = \dot{\omega}_k \quad k = 1, \dots, N_s. \quad (4)$$

Here, ρ is the density, $(u_i)_{i=1,2,3}$ is the velocity vector in Cartesian coordinates, E is the specific total energy, P is the pressure, and Y_k is the mass fraction for the k^{th} species. Additionally, N_s is the total number of species in the flow, τ_{ij} is the viscous stress tensor, q_i is the heat flux vector, and $V_{k,i}$ and $\dot{\omega}_k$ are the diffusion velocity component and reaction rate of the k^{th} species, respectively. The thermally perfect gas equation of state is used to relate the thermodynamic quantities through: $P = \rho RT$. Here, T is the temperature, and R denotes the mixture gas constant. The thermodynamic properties such as specific heats are obtained from classical temperature-dependent curve fits.

In the above equations, the heat-flux vector q_i , and the viscous stress tensor, τ_{ij} , are given by

$$q_i = -\lambda(T) \frac{\partial T}{\partial x_i} + \rho \sum_{k=1}^{N_s} h_k Y_k V_{i,k}, \quad \tau_{ij} = 2\mu(T)(S_{ij} - \frac{1}{3}S_{kk}\delta_{ij}), \quad (5)$$

where $S_{ij} = \frac{1}{2}(\frac{\partial u_i}{\partial x_j} + \frac{\partial u_j}{\partial x_i})$ is the strain-rate tensor, μ is the viscosity, λ is the thermal conductivity, and h_k is the specific enthalpy of the k^{th} species. The transport properties and the diffusion coefficient for species are obtained through the well-known mixture-averaged formulation [27]. The above system of conservation equations is complete after the specification of the initial and boundary conditions specific to a configuration.

B. Two-Scale Decomposition

The TLS model uses scale separation of any variable $\psi(\mathbf{x}, t)$ into its LS and SS components. Here, the LS function is denoted by \mathcal{L}^Δ and although it can be defined in many ways, in the TLS model it is defined on the underlying LS grid G^Δ . Thus, $\psi(\mathbf{x}, t) = \psi^L(\mathbf{x}, t) + \psi^S(\mathbf{x}, t)$, where superscripts ‘L’ and ‘S’ denote large- and small-scale components of $\psi(\mathbf{x}, t)$, respectively. The LS field is defined as [14]:

$$\psi^L(\mathbf{x}, t) = \mathcal{L}^\Delta \psi(\mathbf{x}, t) = \mathcal{I}^\Delta \circ \mathcal{S}^\Delta [\psi(\mathbf{x}, t)], \quad (6a)$$

$$S^\Delta : \psi(\mathbf{x}, t) \rightarrow \psi^L(\mathbf{x}_k, t), \quad \mathcal{I}^\Delta : \psi^L(\mathbf{x}_k, t) \rightarrow \psi^L(\mathbf{x}, t), \quad \mathbf{x}_k \in G^\Delta \equiv \{\mathbf{x}_1, \dots, \mathbf{x}_N\} \subset \Omega, \quad (6b)$$

where, the LS function \mathcal{L}^Δ is the application of a local averaging operator S^Δ followed by an interpolation operator \mathcal{I}^Δ with \mathbf{x}_k representing the nodes corresponding to the LS grid. Applying S^Δ on $\psi(\mathbf{x}, t)$ yields a discrete representation of the LS field denoted by $\psi^L(\mathbf{x}_k, t)$, which is defined at \mathbf{x}_k . This is then interpolated into the SS (finer) grid to obtain a continuous representation of the LS field denoted by $\psi^L(\mathbf{x}, t)$. Once the continuous representation of the LS field is obtained, the corresponding SS field (denoted by ψ^S) is obtained. The SS grid is much finer than the LS grid and is chosen to ensure the resolution of the relevant length scales in a manner similar to DNS. The scale decomposition applied to the mixture fraction field is shown in Fig. 1(a).

In the present study, we follow the formulation described in a past study, where the TLS model was extended to compressible flows. In this approach, the TLS scale decomposition is expressed as $\psi = \tilde{\psi}^L + \psi''^S$, where $\tilde{\psi}^L$ is the Favre density-weighted LS field expressed as: $\tilde{\psi}^L = \frac{(\rho\psi)^L}{\rho^L}$.

C. TLS Equations

Applying the two-scale decomposition discussed in Sec. II.B, leads to the following LS equations for conservation of mass, momentum, energy, and species mass equations:

$$\frac{\partial \rho^L}{\partial t} + \frac{\partial}{\partial x_i} [\rho u_i]^L = 0, \quad (7)$$

$$\frac{\partial \rho^L \tilde{u}_i^L}{\partial t} + \frac{\partial}{\partial x_j} [(\rho u_i u_j)^L + P^L \delta_{ij} - \tilde{\tau}_{ij}^L] = 0, \quad (8)$$

$$\frac{\partial \rho^L \tilde{E}^L}{\partial t} + \frac{\partial}{\partial x_i} [(\rho E + P) u_i]^L + \tilde{q}_i^L - \tilde{u}_j^L \tilde{\tau}_{ij}^L = 0, \quad (9)$$

$$\frac{\partial \rho^L \tilde{Y}_k^L}{\partial t} + \frac{\partial}{\partial x_i} [\rho Y_k (u_i + V_{k,i})]^L = \dot{\omega}_k^L, \quad k = 1, \dots, N_s. \quad (10)$$

The corresponding SS equations are given by

$$\frac{\partial \rho^S}{\partial t} + \frac{\partial}{\partial x_i} [\rho u_i] = \mathcal{E}^L, \quad (11)$$

$$\frac{\partial}{\partial t} (\rho u_i''^S + \rho^S \tilde{u}_i^L) + \frac{\partial}{\partial x_i} [(\rho u_i u_j + P^S \delta_{ij} - \tilde{\tau}_{ij}''^S)] = \mathcal{F}^L, \quad (12)$$

$$\frac{\partial}{\partial t} (\rho \tilde{E}''^S + \rho^S \tilde{E}^L) + \frac{\partial}{\partial x_i} [(\rho E + P) u_i + \tilde{q}_i''^S - \tilde{u}_j^L \tilde{\tau}_{ij}''^S - \tilde{u}_j''^S \tilde{\tau}_{ij}^L - \tilde{u}_j''^S \tilde{\tau}_{ij}''^S] = \mathcal{G}^L, \quad (13)$$

$$\frac{\partial}{\partial t} (\rho \tilde{Y}_k''^S + \rho^S \tilde{Y}_k^L) + \frac{\partial}{\partial x_i} [\rho Y_k (u_i + V_{k,i})] = \dot{\omega}_k^S + \mathcal{H}_k^L, \quad k = 1, \dots, N_s. \quad (14)$$

The terms \mathcal{E}^L , \mathcal{F}^L , \mathcal{G}^L , and \mathcal{H}_k^L couple the LS and SS fields in the mass, momentum, energy, and species mass equations, respectively. These terms are given by

$$\mathcal{E}^L = \frac{\partial}{\partial x_i} [\rho u_i]^L, \quad \mathcal{F}^L = \frac{\partial}{\partial x_j} [\rho u_i u_j]^L, \quad \mathcal{G}^L = \frac{\partial}{\partial x_i} [(\rho E + P) u_i]^L, \quad \mathcal{H}_k^L = \frac{\partial}{\partial x_i} [\rho Y_k (u_i + V_{k,i})]^L, \quad k = 1, \dots, N_s. \quad (15)$$

The above LS and SS equations when combined and expressed in 3D recover the DNS equations, thus offering no computational advantage. In the TLS model, an approximate formulation of the SS equations is obtained to address the computational cost issue, which is discussed next.

D. Modeling of SS Equations

In the TLS model, a two-scale strategy is employed as shown in Fig. 1(b). While the LS equations are solved on a 3D grid using a conventional solver, the SS equations are solved on a collection of three orthogonal 1D lines embedded within the LS grid. The SS grid is chosen to resolve all the smallest spatial scales of interest along the respective direction, and a modeled form of the SS equations is solved on these 1D lines. As the SS equations are solved along the three 1D orthogonal lines, multiple realizations of the SS field are obtained. For example, there is one equation for a SS

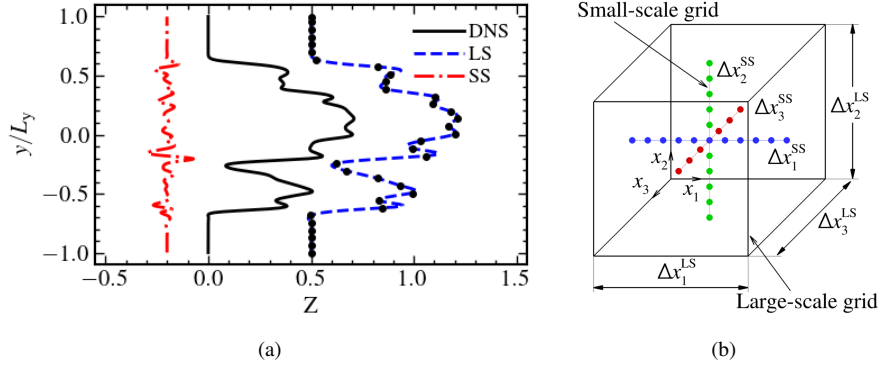


Fig. 1 Illustration of the scale decomposition showing DNS, discrete LS, continuous LS, and SS mixture fraction fields (a) and Sketch of 1D SS lines embedded in the 3D LS grid along three-orthogonal directions (b).

scalar field along each orthogonal direction. Thus, in a given LS grid there are three realizations of the SS scalar field, which are ensemble-averaged to recover the SS scalar field.

Solving the SS equations along each of the 1D lines requires assumptions that primarily impact how the derivatives in the transverse directions (to the 1D direction) are modeled. The rationale and the justification used for the velocity and scalar fields were discussed earlier in the context of incompressible turbulent flows with scalar mixing, and are, therefore, not repeated here, for brevity. For reacting flows, which is of interest in the present study, two assumptions are employed. These assumptions for a scalar field ϕ are given by

- 1) the SS second-order derivative along the 1D line l_k for the SS scalar field ϕ^S is modeled as the average sum of the SS second-order derivatives along all three orthogonal directions through:

$$\frac{\partial^2 \phi^S}{\partial x_k \partial x_k} = \frac{1}{3} \sum_{j=1}^3 \frac{\partial^2 \phi^S}{\partial x_j^2}. \quad (16)$$

Here ‘ k ’ is a free index and refers to the line l_k , which is parallel to the corresponding coordinate x_k ($k = 1, 2,$ and 3).

- 2) the SS contribution to the advection term from the SS scalar field is neglected in the transverse direction ($j \neq k$) to the line l_k :

$$\frac{\partial}{\partial x_j} [(\rho^L + \rho^S)(\tilde{u}_j^L + u_j''^S)(\tilde{\phi}^L + \phi''^S)]^S = \frac{\partial}{\partial x_j} [(\rho^L + \rho^S(l_k))(\tilde{u}_j^L + u_j''^S(l_k))(\tilde{\phi}^L + \phi''^S)(l_k)]^S. \quad (17)$$

These two assumptions lead to a simplified form of the 1D SS equations, thus leading to a significant computational cost reduction. The approximated 1D SS equations along line l_k are given by

$$\frac{\partial \rho^S}{\partial t} + \frac{\partial}{\partial x_i} [\rho(l_k) u_i(l_k)] = \mathcal{E}^L(l_k), \quad (18)$$

$$\frac{\partial}{\partial t} (\rho u_i''^S + \rho^S \tilde{u}_i^L) + \frac{\partial}{\partial x_j} [(\rho(l_k) u_i(l_k) u_j(l_k)) + P^S(l_k) \delta_{ij} - \tilde{\tau}_{ij}''^S(l_k)] = \mathcal{F}^L(l_k), \quad (19)$$

$$\begin{aligned} \frac{\partial}{\partial t} (\rho \tilde{E}''^S + \rho^S \tilde{E}^L) + \frac{\partial}{\partial x_i} [(\rho(l_k) E(l_k) + P(l_k)) u_i(l_k) + \tilde{q}_i''^S(l_k) \\ - \tilde{u}_j''^L \tilde{q}_i''^S(l_k) - \tilde{u}_j''^S(l_k) \tilde{\tau}_{ij}''^L - \tilde{u}_j''^S(l_k) \tilde{\tau}_{ij}''^S(l_k)] = \mathcal{G}^L(l_k), \end{aligned} \quad (20)$$

$$\frac{\partial}{\partial t} (\rho \tilde{Y}_m''^S + \rho^S \tilde{Y}_m^L) + \frac{\partial}{\partial x_i} [\rho(l_k) Y_m(l_k) (u_i(l_k) + V_{m,i}(l_k))] = \dot{\omega}_m^S(l_k) + \mathcal{H}_m^L(l_k), \quad m = 1, \dots, N_s. \quad (21)$$

III. Computational Approach and Setup

In this section, we first describe the numerical methodology used to perform DNS of the case considered in this study. Afterward, the canonical non-premixed jet flame configuration is discussed.

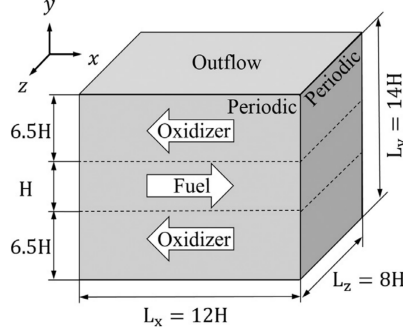


Fig. 2 Schematic of the turbulent non-premixed flame configuration.

A. Numerical Methodology

The governing equations described in Sec. II.A are solved using a well-established 3D parallel, multi-species compressible reacting flow solver, referred to as AVF-LESLIE [28, 29]. It is a multi-physics simulation tool capable of performing DNS and LES of reacting/non-reacting flows. It has been extensively used in the past to study a wide variety of flow conditions, including acoustic flame-vortex interaction, premixed flame turbulence interaction, non-premixed combustion, and compressible turbulence [26, 28–31].

The solver utilizes a finite volume-based spatial discretization of the governing equations in their conservative form on a structured grid using the generalized curvilinear coordinates. The spatial discretization is based on the well-known second-order accurate MacCormack scheme [32]. The time integration of the semi-discrete system of equations is performed by an explicit second-order accurate scheme. The solver can handle arbitrarily complex finite-rate chemical kinetics. The mixture-averaged transport properties, the finite-rate kinetics source terms, and the thermally perfect gas-based thermodynamic properties are obtained using the Cantera software [33]. The parallelization of the solver is based on the standard domain decomposition technique based on the message-passing interface library. The chemical kinetics employed in this study is a 21-step, 11-species non-stiff mechanism developed by Hawkes et al., which has been used previously in both DNS [34] and LES studies [25].

B. Computational Setup

A schematic of the non-premixed flame configuration is shown in Fig. 2. We consider the flow with a characteristic jet velocity $U = 100$ m/s at a pressure $P = 1$ atm. The flow configuration comprises an inner fuel jet (50% CO, 10% H_2 , and 40% N_2 by volume) and an outer oxidizer stream (25% O_2 and 75% N_2 by volume), which are counter-flowing in the streamwise direction. The jet has a Reynolds number (Re_{jet}) of 2315 and a Damköhler number (Da) of 0.01, which is low enough to induce local extinction during turbulence-chemistry interaction. The extent of the computational domain is $L_x \times L_y \times L_z = 12H \times 14H \times 8H$, where $H = 0.96$ mm is the initial width of the fuel jet. The simulations in this study employ about 18 uniformly spaced points along H , which leads to approximately 2.1M grid points total, with a minimum resolution of approximately 4η .

The reacting flow field is initialized with a laminar flamelet solution [35] at a bulk strain rate $\kappa = 0.75\kappa_q$, where $\kappa_q = 1295s^{-1}$ is the extinction bulk strain rate. Here, κ_q is obtained by gradually increasing the bulk strain rate in the laminar flamelet calculation until extinction occurs. To allow for the evolution of shear layer turbulence, broadband isotropic turbulence is superimposed on the mean flow with an initial integral length-scale of $H/3$, and turbulence intensity of $0.05U$. A periodic boundary condition is specified along the streamwise and spanwise directions, whereas a perfectly non-reflecting, characteristic-based outflow boundary condition is used in the transverse direction. The characteristic transient jet time is defined as $t_j = H/U$ and the simulations are conducted up to $40t_j$ to capture both the extinction and re-ignition events.

IV. Results

A. Instantaneous Reacting Flow Features

The spatial evolution of the flame structure at local extinction and re-ignition time instants is shown in Fig. 3 (a-b). The flame location is identified by using iso-lines of $Z = Z_{st}$, where $Z = (sY_F - Y_{O,0}) / (sY_{F,0} + Y_{O,0})$ is the mixture fraction and Z_{st} is the stoichiometric mixture fraction. Here, s is the stoichiometric air-fuel ratio, Y_F is the fuel

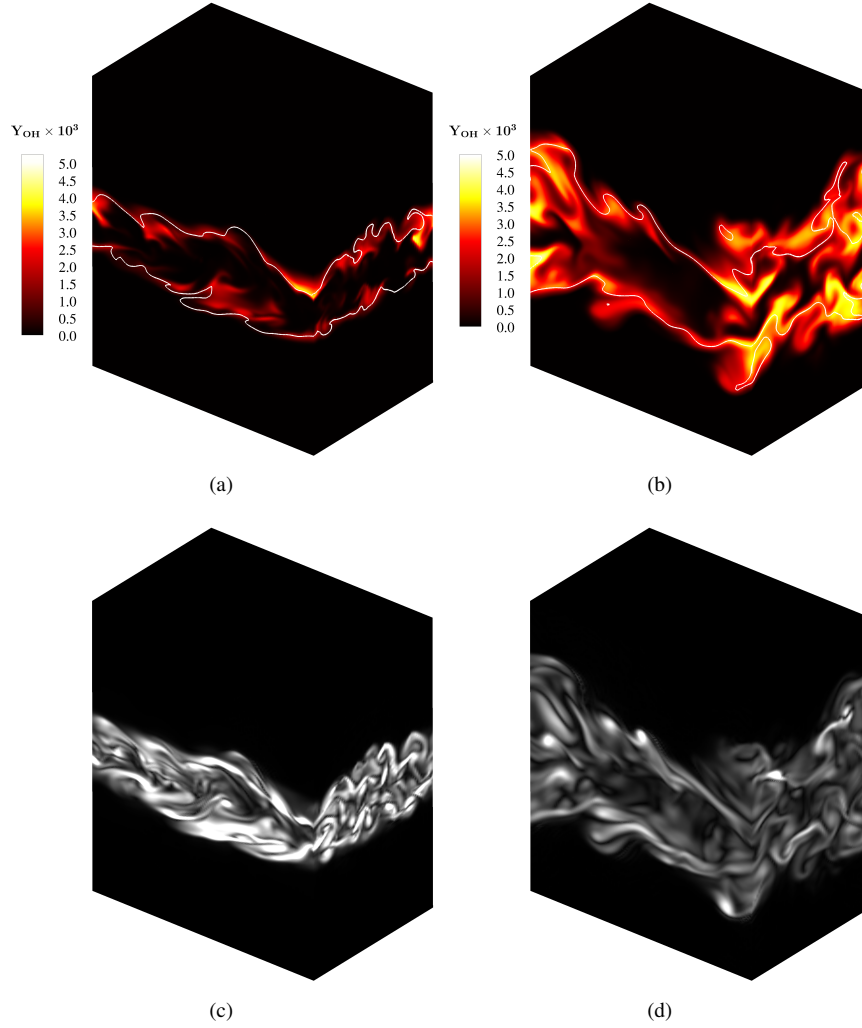


Fig. 3 Contours of OH mass fraction overlaid with the stoichiometric mixture fraction (upper) and vorticity magnitude (lower) at times corresponding to local extinction (left) and re-ignition (right).

mass fraction, Y_O is the oxidizer mass fraction, $Y_{F,0}$ is the fuel mass fraction at fuel stream inlet, and $Y_{O,0}$ is the oxidizer mass fraction at oxidizer stream inlet.

At $20t_j$ only a few distinct OH pockets survive and bind to the stoichiometric surfaces suggesting that local extinction has been reached in most of the shear layer regions. However, at $40t_j$, the values of OH mass fraction increase sharply in most regions inside the shear layers surrounding the stoichiometric surfaces, thus indicating the approach of re-ignition. Some of the disconnected small radical pockets observed at $20t_j$ become the source of re-ignition at $40t_j$.

Figure 4 shows the temporal evolution and PDF of the temperature field on the $Z = Z_{st}$ iso-surface. The mean temperature starts at approximately 1600 K, and then gradually decreases to ~ 1180 K at $20t_j$, and then gradually increases to ~ 1600 K at $40t_j$. This evolution of the mean temperature clearly shows the approach towards local extinction followed by a subsequent re-ignition. The most probable temperatures in the PDF plots (see Fig. 4) follow the temporal evolution of mean temperature. PDFs at re-ignition are much narrower than those at local extinction, which indicates that even at local extinction, there are some pockets of gas in a fully burning state.

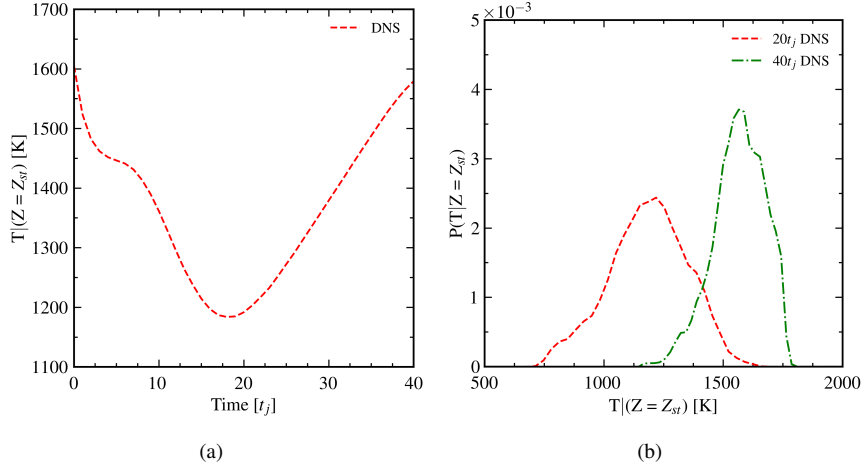


Fig. 4 (a) Temporal evolution of mean temperature on the stoichiometric surface and (b) PDF of temperature on the stoichiometric surface at local extinction ($20t_j$) and re-ignition ($40t_j$).

Table 1 Correlation coefficient of $M_{\phi,2}^v$ with respect to $E_{\phi,2}^v$ along line l_2 for $\phi = Z$ and $\phi = u$ at extinction and re-ignition using different LS grids.

LS grid	$t = 20t_j$		$t = 40t_j$	
	$\phi = Z$	$\phi = u$	$\phi = Z$	$\phi = u$
LS ^{4Δ}	0.93	0.90	0.93	0.89
LS ^{8Δ}	0.88	0.86	0.89	0.87
LS ^{16Δ}	0.83	0.79	0.84	0.80

B. Assessment of TLS Modeling Assumptions

In this section, we assess the validity of the two assumptions discussed in Sec. II.D employed by the TLS model to obtain the approximated 1D SS equations. The modeling assumptions are assessed along line l_2 , which is oriented along the vertical direction.

The first TLS model assumption discussed in Sec. II.D corresponds to the reduction of the 3D SS second-order derivatives along a particular 1D line. According to this assumption, the difference between the SS second-order derivatives of a field variable ϕ in a particular direction on the 1D line l_k and the averaged sum of the SS second-order derivatives in all three directions is equal to zero, i.e., $V_{\phi,k} = 0$, where $V_{\phi,k} = \sum_{j=1}^3 \frac{1}{3} \frac{\partial^2 \phi^S}{\partial x_j^2} - \frac{\partial^2 \phi^S}{\partial x_k^2}$. Here, k is not a repeated index.

To examine the behavior of the SS second-order derivative terms, we examine the joint PDFs of the modeled $\left(M_{\phi,k}^v = \sum_{j=1}^3 \frac{1}{3} \frac{\partial^2 \phi^S}{\partial x_j^2}\right)$ and the exact $\left(M_{\phi,k}^v = \frac{\partial^2 \phi^S}{\partial x_k^2}\right)$ SS second-order derivative terms along line l_2 . Here, the superscript ‘v’ indicates the contribution of the SS second-order derivative terms to the viscous terms. Figure 5 shows the joint PDFs of $M_{\phi,2}^v$ with respect to $E_{\phi,2}^v$ along line l_2 at $20t_j$ and $40t_j$. The results are examined with $\phi = u$ and $\phi = Z$ which are considered to be the representative fields corresponding to the flow and the scalar fields.

In both cases ($20t_j$ and $40t_j$) and for both field variables, the contours of the joint PDFs exhibit the presence of a peak value near the origin, thus demonstrating the validity of the first modeling assumption. Note that the bisector of the first and the third quadrants implies the model assumption $V_{\phi,k} = 0$, and the events away from the bisector are excluded from the modeling assumption. It is apparent that in both cases, the events with large magnitude $E_{\phi,2}^v$ correlate very well with the event corresponding to a large magnitude of $M_{\phi,2}^v$ with the same sign. The correlation tends to be higher for the mixture fraction field compared to the flow field, which can be attributed to the presence of a mean gradient of the mixture fraction. When the LS grid is coarsened, the contour deviates from the bisector of the first and third quadrants, indicating a reduced correlation between the modeled and the exact quantities. This behavior is clear from

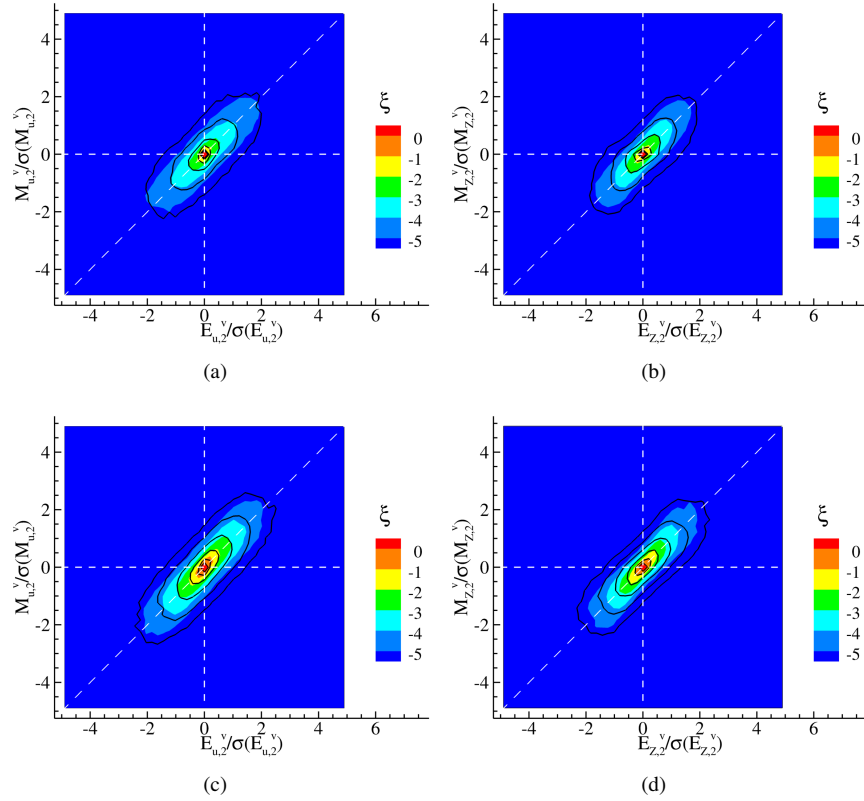


Fig. 5 Transformed joint PDF ($\xi = \ln f$) of $M_{\phi,k}^v$ with respect to $E_{\phi,k}^v$ obtained $t = 20t_j$ (a,b) and $t = 40t_j$ along line l_2 with $\phi = u$ (a, c) and $\phi = Z$ (b, d). The colored and solid curve contours correspond to LS grid resolutions $LS^{4\Delta}$ and $LS^{16\Delta}$, respectively.

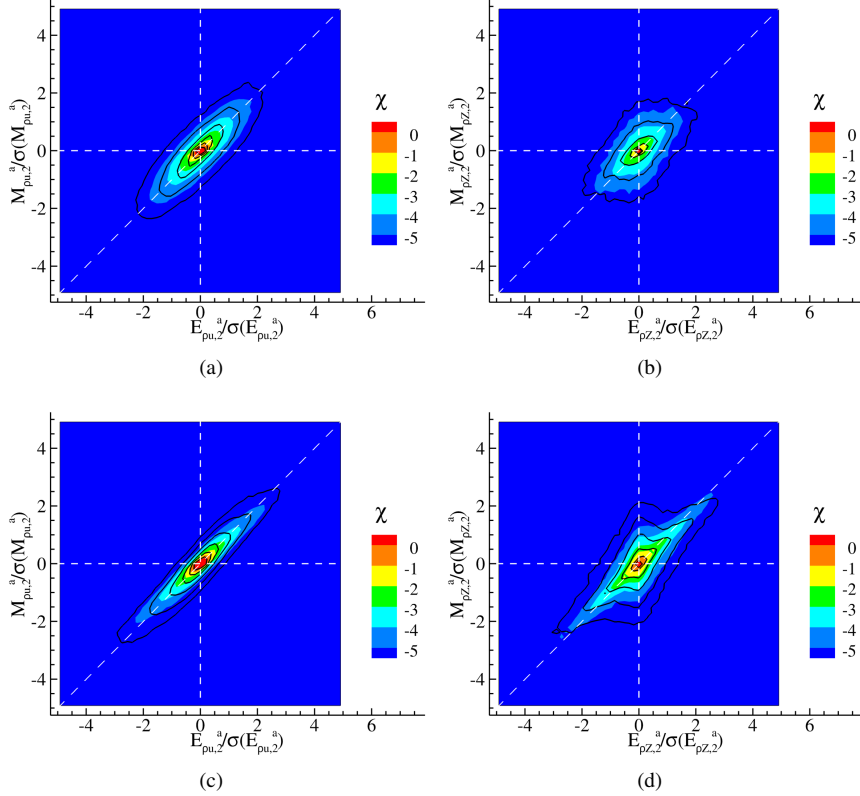


Fig. 6 Transformed joint PDF ($\chi = \ln f$) of $M_{\phi,k}^a$ with respect to $E_{\phi,k}^a$ obtained at $t = 20t_j$ (a,b) and $t = 40t_j$ (c,d) along line l_2 with $\phi = \rho u$ (a, c) and $\phi = \rho Z$ (b, d). The colored and solid curve contours correspond to LS grid resolutions $LS^{4\Delta}$ and $LS^{16\Delta}$, respectively.

the correlation coefficients of $M_{\phi,1}^y$ with respect to $E_{\phi,1}^y$ at various LS grid resolutions summarized in Table 1.

The second assumption made in the TLS model addresses the treatment of the nonlinear advection term. In the solution of the SS equations along a 1D line l_k , the advection of the SS fields in directions orthogonal to l_k are neglected. The assessment of this assumption is performed here for $\phi = \rho Z$ and $\phi = \rho u$ representing the advection of scalar and flow fields. Figure 6 displays the joint PDF of $M_{\phi,2}^a$ and $E_{\phi,2}^a$ at times $t = 20t_j$ and $t = 40t_j$. In all contours, we see a high probability of low-magnitude SS advection, indicating that this term is often relatively negligible. In Fig. 6(a,c) corresponding to the flow field ($\phi = \rho u$), the contour is clustered along the line bisecting quadrants 1 and 3 demonstrating a strong correlation between the modeled and exact quantity both in magnitude and direction. However, this correlation is weaker when considering the scalar field ($\phi = \rho Z$) shown in Fig. 6(b,d). For the scalar field, the effect of grid resolution is apparent, as the case with coarser grid resolution of $LS^{16\Delta}$ is seen to deviate significantly from the diagonal bisector. For both the scalar and flow fields, the correlation between the modeled and exact advection term is stronger at time $t = 40t_j$ relative to $t = 20t_j$. The details of the correlation coefficients between the modeled and exact advection terms are provided in Table 2.

V. Conclusion

In this study, the TLS model, a two-scale modeling strategy originally developed for the simulation of incompressible turbulent flows and passive scalar mixing in such flows, is assessed for its ability to model turbulent non-premixed flames. A key aspect of the TLS model is its ability to capture both large- and small-scale dynamics to approximately represent the dynamics over the entire range of spatial and temporal scales. These features of the TLS method are analyzed through an *a priori* analysis of the DNS dataset to show its capabilities in terms of ability to represent the LS and SS dynamics of the reacting flow field in the physical space.

Table 2 Correlation coefficient of $M_{\phi,2}^a$ with respect to $E_{\phi,2}^a$ along line l_2 for $\phi = \rho Z$ and $\phi = \rho u$ at extinction and reignition using different LS grids.

LS grid	$t = 20t_j$		$t = 40t_j$	
	$\phi = \rho Z$	$\phi = \rho u$	$\phi = Z$	$\phi = u$
LS ^{4Δ}	0.78	0.88	0.92	0.97
LS ^{8Δ}	0.71	0.84	0.84	0.96
LS ^{16Δ}	0.66	0.81	0.75	0.95

The *a priori* analysis is performed using the DNS dataset corresponding to a temporally evolving turbulent non-premixed jet flame which exhibits the approach towards extinction followed by re-ignition. The non-premixed flame is considered at atmospheric pressure with a counter-flowing inner fuel jet and outer oxidizer stream at $Re_{jet} = 2315$ and $Da = 0.01$. The scale-decomposition strategy employed by the TLS model showed that the large- and small-scale variations of the flow are appropriately represented in the physical space. The results also showed that the modeling assumptions employed by the TLS model to approximate the 3D SS equations on the 1D orthogonal lines are reasonable. Future studies will focus on performing a *posteriori* assessment of the TLS model for the flames considered in this study.

Acknowledgments

This work is supported in part by a CEACSE grant through the University of Tennessee at Chattanooga (UTC). The computational resources were provided by the UTC Research Institute under grants from the National Science Foundation (Grant Nos. 1925603 and 2201497) and are greatly appreciated.

References

- [1] Gonzalez-Juez, E. D., Kerstein, A. R., Ranjan, R., and Menon, S., "Advances and challenges in modeling high-speed turbulent combustion in propulsion systems," *Prog. Energy Combust. Sci.*, Vol. 60, 2017, pp. 26–67.
- [2] Pitsch, H., "Large-eddy simulation of turbulent combustion," *Annu. Rev. Fluid Mech.*, Vol. 38, 2006, pp. 453–482.
- [3] Fureby, C., "Large eddy simulation modelling of combustion for propulsion applications," *Philosophical Transactions of the Royal Society A: Mathematical, Physical and Engineering Sciences*, Vol. 367, No. 1899, 2009, pp. 2957–2969.
- [4] Colin, O., Ducros, F., Veynante, D., and Poinso, T., "A thickened flame model for large eddy simulations of turbulent premixed combustion," *Phys. of Fluids*, Vol. 12, No. 7, 2000, pp. 1843–1863.
- [5] Boger, M., Veynante, D., Boughanem, H., and Troune, A., "Direct numerical simulation analysis of flame surface density concept for large eddy simulation of turbulent premixed combustion," *Proc. Combust. Inst.*, Vol. 27, 1998, pp. 917–925.
- [6] Klimenko, A. Y., and Bilger, R. W., "Conditional moment closure for turbulent combustion," *Prog. Energy Combust. Sci.*, Vol. 25, No. 6, 1999, pp. 595–687.
- [7] Steiner, H., and Bushe, W., "Large eddy simulation of a turbulent reacting jet with conditional source-term estimation," *Phys. of Fluids*, Vol. 13, No. 3, 2001, pp. 754–769.
- [8] Gao, F., and O'Brien, E. E., "A large-eddy simulation scheme for turbulent reacting flows," *Phys. of Fluids*, Vol. 5, 1993, pp. 1282–1284.
- [9] Fox, R. O., and Raman, V., "A multienvironment conditional probability density function model for turbulent reacting flows," *Phys. of Fluids*, Vol. 16, No. 12, 2004, pp. 4551–4565.
- [10] Echekki, T., Kerstein, A. R., Dreeben, T. D., and Chen, J.-Y., "One-dimensional turbulence simulation of turbulent jet diffusion flames: model formulation and illustrative applications," *Comp. and Fluids*, Vol. 125, No. 3, 2001, pp. 1083–1105.
- [11] Menon, S., and Kerstein, A. R., "The linear-eddy model," *Turbulent Combustion Modeling*, Vol. 95, 2011, pp. 175–222.
- [12] Ranjan, R., Muralidharan, B., Nagaoka, Y., and Menon, S., "Subgrid-Scale Modeling of Reaction-Diffusion and Scalar Transport in Turbulent Premixed Flames," *Combust. Sci. Technol.*, Vol. 188, 2016, pp. 1496–1537.

- [13] Panchal, A., Ranjan, R., and Menon, S., “A comparison of finite-rate kinetics and flamelet-generated manifold using a multiscale modeling framework for turbulent premixed combustion,” *Combustion Science and Technology*, Vol. 191, No. 5-6, 2019, pp. 921–955.
- [14] Kemenov, K., and Menon, S., “Explicit small-scale velocity simulation for high-Re turbulent flows,” *J. Comp. Phys.*, Vol. 220, 2006, pp. 290–311.
- [15] Ranjan, R., and Menon, S., “Two level simulation of Schmidt number effect on passive scalar transport in wall-bounded turbulent flows,” *Physics of Fluids*, Vol. 33, No. 3, 2021, p. 035124.
- [16] Ranjan, R., and Menon, S., “Vorticity, backscatter and counter-gradient transport predictions using two-level simulation of turbulent flows,” *Journal of Turbulence*, Vol. 19, No. 4, 2018, pp. 334–364.
- [17] Kemenov, K., and Menon, S., “Explicit small-scale velocity simulation for high-Re turbulent flows.part 2: Non-homogeneous flows,” *J. Comp. Phys.*, Vol. 222, 2007, pp. 673–701.
- [18] Gungor, A., and Menon, S., “A new two-scale model for large eddy simulation of wall-bounded flows,” *Prog. Aerospace Sci.*, Vol. 46, 2010, pp. 28–45.
- [19] Ranjan, R., and Menon, S., “A multi-scale simulation method for high Reynolds number wall-bounded turbulent flows,” *J. Turbulence*, Vol. 14, 2013, pp. 1–38.
- [20] Ranjan, R., and Menon, S., “On the application of the two-level large-eddy simulation method to turbulent free-shear and wake flows,” *J. Turbulence*, Vol. 16, 2015, pp. 136–166.
- [21] Ranjan, R., “Large-Eddy Simulation of Transition to Turbulence using the Two-Level Simulation Approach,” *AIAA Aviation 2021 Forum*, 2021.
- [22] Young, M., and Ranjan, R., “Two-Level Simulation of Transition to Turbulence in Wall-Bounded Flows,” *APS Division of Fluid Dynamics Meeting Abstracts*, 2021, pp. F11–006.
- [23] Chandrasekhar, H., Ranjan, R., and Menon, S., “On the Assessment of Two-Level Simulation Model for Numerical Study of Compressible Turbulent Scalar Mixing,” *The 17th International Workshop on the Physics of Compressible Turbulent Mixing*, 2022.
- [24] Ranjan, R., “A Priori Assessment of Two-Level Simulation Model for Numerical Investigation of Turbulent Premixed Flames,” *AIAA SCITECH 2023 Forum*, 2023, p. 1691.
- [25] Sen, B. A., Hawkes, E. R., and Menon, S., “Large eddy simulation of extinction and reignition with artificial neural networks based chemical kinetics,” *Combustion and Flame*, Vol. 157, No. 3, 2010, pp. 566–578.
- [26] Yang, S., Ranjan, R., Yang, V., Wenting, S., and Menon, S., “Sensitivity of predictions to chemical kinetics models in a temporally evolving turbulent non-premixed flame,” *Combustion and Flame*, Vol. 183, 2017, pp. 224–241.
- [27] Poinso, T., and Veynante, D., *Theoretical and Numerical Combustion*, 2nd ed., Edwards, Inc., 2005.
- [28] Kim, W., and Menon, S., “Numerical Simulations of Turbulent Premixed Flames in the Thin-Reaction-Zones Regime,” *Combustion Science and Technology*, Vol. 160, 2000, pp. 119–150.
- [29] Sankaran, V., and Menon, S., “Subgrid combustion modeling of 3-D premixed flames in the thin-reaction-zone regime,” *Proc. Combust. Inst.*, Vol. 30, No. 1, 2005, pp. 575–582.
- [30] Bowers, J., Durant, E., and Ranjan, R., “Application of Intrusive and Non-Intrusive Reduced Order Modeling Techniques for Simulation of Turbulent Premixed Flames,” *AIAA Propulsion and Energy 2021 Forum*, 2021, p. 3634.
- [31] Lowery, C., Hasti, V. R., and Ranjan, R., “Characteristics of Non-Equilibrium Turbulence in Couette Flow under Compressible Conditions,” *AIAA AVIATION 2022 Forum*, 2022, p. 4035.
- [32] MacCormack, R. W., “The effect of viscosity in hypervelocity impact cratering,” *J. Space. Rockets*, Vol. 40, No. 5, 2003, pp. 757–763.
- [33] Goodwin, D. G., Moffat, H. K., and Speth, R. L., “Cantera: An Object-oriented Software Toolkit for Chemical Kinetics, Thermodynamics, and Transport Processes,” <http://www.cantera.org>, 2014. Version 2.1.2.
- [34] Hawkes, E. R., Sankaran, R., Sutherland, J. C., and Chen, J. H., “Scalar mixing in direct numerical simulations of temporally evolving plane jet flames with skeletal CO/H₂ kinetics,” *Proc. Combust. Inst.*, Vol. 31, No. 1, 2007, pp. 1633–1640.
- [35] Peters, N., “Laminar diffusion flamelet models in non-premixed turbulent combustion,” *Progress in Energy and Combustion Science*, Vol. 10, No. 3, 1984, pp. 319–339.